

# Possible thermochemical disequilibrium in the atmosphere of the exoplanet GJ 436b

Kevin B. Stevenson<sup>1</sup>, Joseph Harrington<sup>1</sup>, Sarah Nymeyer<sup>1</sup>, Nikku Madhusudhan<sup>2</sup>, Sara Seager<sup>2</sup>, William C. Bowman<sup>1</sup>, Ryan A. Hardy<sup>1</sup>, Drake Deming<sup>3</sup>, Emily Rauscher<sup>4</sup> & Nate B. Lust<sup>1</sup>

The nearby extrasolar planet GJ 436b—which has been labelled as a ‘hot Neptune’—reveals itself by the dimming of light as it crosses in front of and behind its parent star as seen from Earth. Respectively known as the primary transit and secondary eclipse, the former constrains the planet’s radius and mass<sup>1,2</sup>, and the latter constrains the planet’s temperature<sup>3,4</sup> and, with measurements at multiple wavelengths, its atmospheric composition. Previous work<sup>5</sup> using transmission spectroscopy failed to detect the 1.4- $\mu\text{m}$  water vapour band, leaving the planet’s atmospheric composition poorly constrained. Here we report the detection of planetary thermal emission from the dayside of GJ 436b at multiple infrared wavelengths during the secondary eclipse. The best-fit compositional models contain a high CO abundance and a substantial methane ( $\text{CH}_4$ ) deficiency relative to thermochemical equilibrium models<sup>6</sup> for the predicted hydrogen-dominated atmosphere<sup>7,8</sup>. Moreover, we report the presence of some  $\text{H}_2\text{O}$  and traces of

$\text{CO}_2$ . Because  $\text{CH}_4$  is expected to be the dominant carbon-bearing species, disequilibrium processes such as vertical mixing<sup>9</sup> and polymerization of methane<sup>10</sup> into substances such as ethylene may be required to explain the hot Neptune’s small  $\text{CH}_4$ -to-CO ratio, which is at least  $10^5$  times smaller than predicted<sup>6</sup>.

Using the Spitzer Space Telescope<sup>11</sup>, the Spitzer Exoplanet Target of Opportunity program observed multiple secondary eclipses at wavelengths of 3.6, 4.5, 5.8, 8.0, 16 and 24  $\mu\text{m}$ . Previous analyses<sup>3,4</sup> of our 8.0- $\mu\text{m}$  secondary eclipse data confirm an eccentric orbit around GJ 436, which is a cool, M-dwarf star. Standard image calibration and photometry produced light curves (tables of system flux versus time at each wavelength) that are available as Supplementary Information, as are details of centring and photometry. Some channels have well documented systematic effects that our Metropolis-Hastings Markov-chain Monte Carlo (MCMC) model<sup>12</sup> fits simultaneously with the eclipse parameters. Systematics include positional

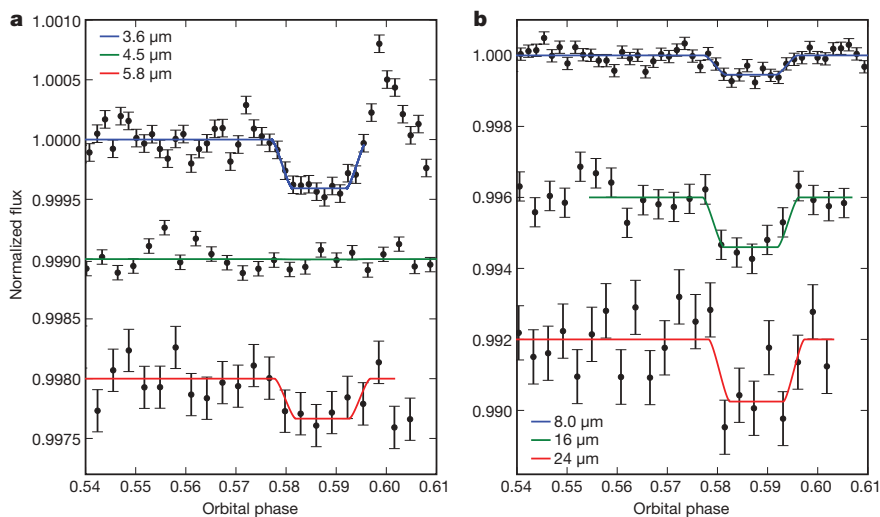


**Figure 1 | Secondary eclipses of GJ 436b at six Spitzer wavelengths.** The flux values are corrected for sensitivity effects, normalized to the system brightness, and vertically separated for ease of comparison. **a**, Binned 3.6-, 4.5- and 5.8- $\mu\text{m}$  data (with  $1\sigma$  error bars), **b**, binned 8.0-, 16- and 24- $\mu\text{m}$  data (with  $1\sigma$  error bars), both with best-fit models and for orbital phases greater than 0.54. Note the different vertical scales used in each panel. The phase calculation uses an ephemeris time of Julian date 2,454,222.61588 and a period of 2.6438986 days (ref. 16). Because the planet passes behind the star, we ignore stellar limb darkening and use the uniform-source equations<sup>29</sup> for the eclipse shape. The position sensitivity model used either a quadratic<sup>13</sup> or a cubic function in the two spatial variables, including the cross terms to account for any correlation. An asymptotically constant exponential

function<sup>14</sup> models the time-varying sensitivity. The 3.6- and 4.5- $\mu\text{m}$  channels exhibit strong position sensitivity while the 5.8- $\mu\text{m}$  channel reveals a weak correlation with pixel position. The unmodelled region at 3.6  $\mu\text{m}$  may be the result of stellar activity<sup>30</sup>, a similar region at 5.8  $\mu\text{m}$  is unmodelled for reasons presented in Supplementary Information. We detect no eclipse at 4.5  $\mu\text{m}$ , but constrain the flux modulation at its  $3\sigma$  upper bound by fixing the secondary eclipse phase to the mean weighted value of the other channels. We use asymptotically constant exponential and linear functions to model the time-varying sensitivities at 8.0 and 16  $\mu\text{m}$ , respectively. Our 8.0- $\mu\text{m}$  analysis agrees with prior analyses<sup>3,4</sup> but we obtain a slightly higher brightness temperature (Table 1) due, in part, to a more recent Kurucz model<sup>24</sup>. No correction is necessary at 24  $\mu\text{m}$ .

<sup>1</sup>Planetary Sciences Group, Department of Physics, University of Central Florida, Orlando, Florida 32816, USA. <sup>2</sup>Department of Physics and Department of Earth, Atmospheric and Planetary Sciences, Massachusetts Institute of Technology, Cambridge, Massachusetts 02139, USA. <sup>3</sup>Planetary Systems Laboratory, NASA Goddard Space Flight Center, Greenbelt, Maryland 20771, USA. <sup>4</sup>Department of Astronomy, Columbia University, New York, New York 10027, USA.

**Table 1 | Eclipse parameters and brightness temperatures**

Channel ( $\mu\text{m}$ )	Eclipse midpoint (BJD - 2454000)	Eclipse duration (orbits)	Flux modulation (%)	Brightness temperature (K)
3.6	496.4888 $\pm$ 0.0010	0.0192 $\pm$ 0.0008	0.041 $\pm$ 0.003	1,120 $\pm$ 20
4.5	499.1330	0.0191	<0.010*	<700
5.8	501.778 $\pm$ 0.005	0.0191	0.033 $\pm$ 0.014	720 $\pm$ 110
8.0	282.3331 $\pm$ 0.0016	0.0186 $\pm$ 0.0014	0.054 $\pm$ 0.008	740 $\pm$ 40
16	477.981 $\pm$ 0.003	0.0191 $\pm$ 0.0023	0.140 $\pm$ 0.027	980 $\pm$ 130
24	470.053 $\pm$ 0.002	0.0191	0.175 $\pm$ 0.041	960 $\pm$ 170

BJD, barycentric Julian date; 1 orbit = 2.6438986 days. Eclipse duration is measured from start of ingress ( $t_i$ ) to end of egress ( $t_e$ ). Flux modulation is one minus in-eclipse flux divided by out-of-eclipse flux. Brightness temperature is the temperature of a similar blackbody that produces the same flux as the source in a given wavelength bandpass. The eclipses at 3.6, 8.0 and 16  $\mu\text{m}$  are clear enough to fit durations; their weighted mean (72.6  $\pm$  2.6 min) fixes the durations for the other wavelengths. We fix the ingress/egress times to 16 min (ref. 23) for all channels. Varying them produces equivalent times within the errors but degrades the overall fit quality. The Supplementary Tables and Supplementary Figures contain complete parameter results. The brightness temperature calculation<sup>14</sup> refers the flux modulation to a stellar spectrum model, which is interpolated from a grid of Kurucz models<sup>24</sup> using GJ 436's temperature (3,684  $\pm$  71 K), log surface gravity (4.80  $\pm$  0.10), and metallicity (-0.32  $\pm$  0.12 dex)<sup>2,25</sup>. A Monte Carlo method computes the uncertainty in brightness temperature by varying the flux modulation and stellar parameters. The differing brightness temperatures at 3.6 and 4.5  $\mu\text{m}$  suggest that these two wavelengths measure two different pressure levels; indeed, Supplementary Fig. 5 shows that the 4.5- $\mu\text{m}$  channel has an additional contribution from higher up in the atmosphere. To explain the 400 K difference in brightness temperatures, the model requires a very low concentration of methane.

\*  $3\sigma$  upper limit.

sensitivity variation<sup>13</sup> at 3.6, 4.5 and 5.8  $\mu\text{m}$ , where the measured flux correlates with the sub-pixel location of the stellar centre, and time-varying sensitivity<sup>14</sup> at 4.5, 5.8, 8.0 and 16  $\mu\text{m}$ . Responsivity of the 24- $\mu\text{m}$  channel is relatively stable<sup>15</sup>. Figure 1 shows the observed secondary eclipses with best-fit models, and Table 1 presents the relevant eclipse parameters.

The phase of secondary eclipse imposes a tight constraint on the planet's eccentricity,  $e$ , and argument of periapsis,  $\omega$ . Using the secondary eclipse times listed in Table 1, in addition to published transit<sup>16</sup> and radial-velocity data<sup>17</sup>, a single-planet Keplerian orbit for GJ 436b has a period of 2.6438983  $\pm$  0.0000016 days and an ephemeris time of Julian date 2,454,222.61587  $\pm$  0.00012 (all errors are  $1\sigma$ ). These are nearly identical to the published results<sup>16</sup>, which do not consider secondary eclipses. Using either result, the weighted average of the five measured secondary eclipse phases is 0.5868  $\pm$  0.0003. This significant improvement from previous analyses<sup>3,4</sup> is due to the more precise ephemeris time and the use of multiple secondary eclipses over a long baseline. The weighted average of the minimum eccentricities, defined as  $e_{\text{min}} \approx e \cos(\omega)$ , is 0.1368  $\pm$  0.0004. Using  $\omega = 351 \pm 1.2^\circ$  (ref. 17), we find  $e = 0.1385 \pm 0.0006$ . To compute all of the orbital parameters (Supplementary Information), we used the published results referenced above in addition to the eclipse times presented here. Our best-fit value for  $e$  is 0.1371  $^{+0.0048}_{-0.00013}$ .

Our broadband observations constrain a one-dimensional atmospheric model, using a new temperature and abundance retrieval method<sup>18</sup>. This method searches over a wide parameter space using

a functional form for the pressure–temperature profile (based on prior ‘hot Jupiter’ and Solar System studies), a grid of abundance combinations, and energy conservation. We calculated  $\sim 10^6$  models, which considered both inversion and non-inversion temperature profiles and abundances that varied over several orders of magnitude per constituent. Figure 2 shows two representative models (the red and blue lines) that fit the data, and Table 2 compares them to seven other objects with hydrogen-dominated atmospheres. The red model has a dayside-to-nightside energy redistribution ratio of <0.04; the blue model favours a more efficient distribution ratio of <0.31. The red model fits the data better.

Chemical equilibrium predicts  $\text{H}_2$ ,  $\text{H}_2\text{O}$ ,  $\text{CH}_4$ ,  $\text{CO}$  and  $\text{NH}_3$  to be the most abundant molecules in GJ 436b's atmosphere (helium must also be present but contributes minimally to the spectrum and to active chemistry). Conventional chemical composition models predict<sup>6,19</sup> the major emission contributions to come from spectroscopically active  $\text{H}_2\text{O}$ ,  $\text{CH}_4$ , and, to a lesser extent,  $\text{CO}$ , and possibly  $\text{CO}_2$ . In a reduced, hydrogen-dominated atmosphere at  $\sim 700$  K,  $\text{CH}_4$  is thermochemically favoured to be the main carbon-bearing molecule. Assuming solar abundances for the elements and the pressure–temperature profile shown in Supplementary Fig. 5, chemical equilibrium predicts<sup>6</sup> a  $\text{CH}_4$ -to- $\text{H}_2$  mixing ratio of  $7 \times 10^{-4}$  and an  $\text{H}_2\text{O}$  mixing ratio of  $2 \times 10^{-3}$ . However, the strong planetary emission at 3.6  $\mu\text{m}$ , combined with the non-detection at 4.5  $\mu\text{m}$ , calls for a methane abundance that is depleted by a factor of  $\sim 7,000$ . The low  $\text{H}_2\text{O}$  abundance favoured by our red model could,

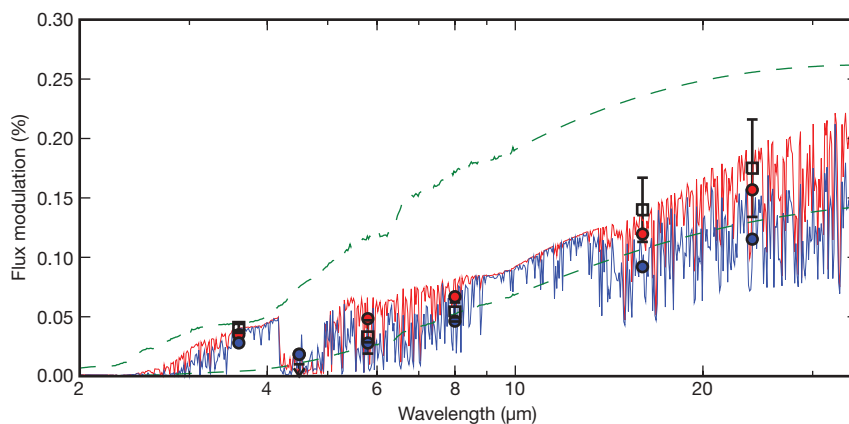


**Figure 2 | Broadband spectrum constraints for GJ 436b.** The two atmospheric models (red and blue lines) have the same temperature structure (shown in Supplementary Fig. 5) and no thermal inversion. The red model has uniform mixing ratios for  $\text{H}_2\text{O}$ ,  $\text{CH}_4$ ,  $\text{CO}$  and  $\text{CO}_2$  of  $3 \times 10^{-6}$ ,  $1 \times 10^{-7}$ ,  $7 \times 10^{-4}$  and  $1 \times 10^{-7}$ , respectively. For the blue model, these are  $1 \times 10^{-4}$ ,  $1 \times 10^{-7}$ ,  $1 \times 10^{-4}$  and  $1 \times 10^{-6}$ . The 3.6- $\mu\text{m}$  channel is the key measurement in terms of constraining the methane abundance. It also limits the amount of  $\text{H}_2\text{O}$  to less than that of  $\text{CO}$ , with little to no energy redistribution. Chemical equilibrium also requires some  $\text{NH}_3$ . The coloured circles are the bandpass-integrated models, the black squares are our data

(with  $1\sigma$  error bars), and the black arrow depicts the  $3\sigma$  upper limit at 4.5  $\mu\text{m}$ . The dashed green curves show blackbody spectra at 650 K (bottom) and 1,050 K (top) divided by the Kurucz stellar spectrum model<sup>24</sup>. The red and blue models have effective (equivalent blackbody) temperatures of 860 K and 790 K, respectively. We need not invoke an internal heat source<sup>3</sup>. Assuming zero albedo and planet-wide redistribution of heat, GJ 436b has an equilibrium temperature ( $T_{\text{eq}}$ , where emitted and absorbed radiation balance for an equivalent blackbody) of 770 K at periapsis. For instantaneous reradiation of absorbed energy at secondary eclipse, the hemispheric effective temperature is 800 K and the peak temperature is 1,030 K.

**Table 2 | Atmospheric data for various planets**

Planet	H <sub>2</sub> O	CH <sub>4</sub>	CO	CO <sub>2</sub>	T <sub>eff</sub> (K)	CH <sub>4</sub> /CO
HD 209458b <sup>18</sup> (Spitzer broadband)	10 <sup>-8</sup> -10 <sup>-5</sup>	(4 × 10 <sup>-8</sup> )-(3 × 10 <sup>-2</sup> )	≥4 × 10 <sup>-4</sup>	(0.4-7) × 10 <sup>-8</sup>	1,310-1,690	10 <sup>-7</sup> -10 <sup>2</sup>
HD 189733b <sup>18</sup> (Spitzer broadband)	10 <sup>-5</sup> -10 <sup>-3</sup>	≤2 × 10 <sup>-6</sup>	(7 × 10 <sup>-8</sup> )-(2 × 10 <sup>-2</sup> )	(0.07-7) × 10 <sup>-5</sup>	1,480-1,560	10 <sup>-10</sup> -10
HD 189733b <sup>26</sup> (HST/NICMOS)	10 <sup>-4</sup> -10 <sup>-3</sup>	≤1 × 10 <sup>-7</sup>	(1-3) × 10 <sup>-4</sup>	(0.1-1) × 10 <sup>-5</sup>	NA	≤10 <sup>-3</sup>
GJ 436b (red model)	3 × 10 <sup>-6</sup>	1 × 10 <sup>-7</sup>	7 × 10 <sup>-4</sup>	1 × 10 <sup>-7</sup>	860	~10 <sup>-4</sup>
GJ 570D <sup>2</sup>	7 × 10 <sup>-4</sup>	5 × 10 <sup>-4</sup>	2 × 10 <sup>-6</sup>	NA	800	~10 <sup>2</sup>
GJ 436b (blue model)	1 × 10 <sup>-4</sup>	1 × 10 <sup>-7</sup>	1 × 10 <sup>-4</sup>	1 × 10 <sup>-6</sup>	790	~10 <sup>-3</sup>
Jupiter <sup>27</sup>	(0.2-2) × 10 <sup>-8*</sup>	2.1 × 10 <sup>-3</sup>	1.6 × 10 <sup>-9</sup>	≤3 × 10 <sup>-9</sup>	110	~10 <sup>6</sup>
Saturn <sup>27</sup>	(0.2-2) × 10 <sup>-8*</sup>	4.5 × 10 <sup>-3</sup>	1 × 10 <sup>-9</sup>	3 × 10 <sup>-10</sup>	100	~10 <sup>6</sup>
Uranus <sup>28</sup>	Ice	2.3 × 10 <sup>-2</sup>	≤1.2 × 10 <sup>-8</sup>	NA	60	~10 <sup>6</sup>
Neptune <sup>28</sup>	Ice	2.9 × 10 <sup>-2</sup>	~1 × 10 <sup>-6</sup>	NA	60	~10 <sup>4</sup>

Values given under headings H<sub>2</sub>O, CH<sub>4</sub>, CO and CO<sub>2</sub> are mixing ratios relative to molecular hydrogen. T<sub>eff</sub>, effective temperature; HST/NICMOS, Hubble Space Telescope Near Infrared Camera and Multi-Object Spectrometer. The planets are ordered in descending effective temperature. Chemical equilibrium predicts a roughly increasing CH<sub>4</sub>-to-CO ratio. GJ 436b does not follow this general trend, as seen in the rightmost column. Its CH<sub>4</sub>-to-H<sub>2</sub> mixing ratio is >10<sup>3</sup> times less than that of a brown dwarf of similar temperature and its CH<sub>4</sub>-to-CO ratio is >10<sup>2</sup> times less. Excess CO may be the result of relatively strong vertical mixing<sup>9</sup>. A significant fraction of the methane may have polymerized into hydrocarbons<sup>10</sup>, resulting in a shortage in observed CH<sub>4</sub>. For comparison, GJ 436b's required methane mixing ratio of 10<sup>-7</sup> is about 10<sup>3</sup> times less than that on Uranus and Neptune, 10<sup>4</sup> times less than that on Jupiter and Saturn, and ~20 times less than that on Earth, where methane is oxidized, not polymerized. NA, not available.

\* Above cloud.

in principle, result from carbon and oxygen abundances that are ~0.01 times solar values; however, the resulting CH<sub>4</sub> mixing ratio would still be too high, by two orders of magnitude, to explain the data.

Methane absorbs strongly in the 3.6- $\mu$ m band. CO and CO<sub>2</sub> have absorption features at 4.5  $\mu$ m, CO<sub>2</sub> being the stronger absorber. The high flux at 3.6  $\mu$ m suggests very low absorption due to methane, while the low flux at 4.5  $\mu$ m implies high absorption due to CO and/or CO<sub>2</sub>. The degeneracy between the two molecules is solved by the low CO<sub>2</sub> concentration allowed at 16  $\mu$ m. The absence of observed flux in the 4.5- $\mu$ m channel thus requires large amounts of CO, which is not expected in such a reduced atmosphere under thermochemical equilibrium, and makes a future detection at 4.5  $\mu$ m important.

The flux modulation at 3.6  $\mu$ m is our strongest detection, with a signal-to-noise ratio of 12.1, and has been confirmed by an independent analysis. Using 2 $\sigma$  error bars for this observation and the 3 $\sigma$  upper limit at 4.5  $\mu$ m, the low-methane requirement cannot be lifted (this result is relatively insensitive to the remaining wavelengths). An increased methane mixing ratio of 10<sup>-6</sup> would result in a higher blackbody continuum, thus requiring a CO<sub>2</sub> mixing ratio ≥10<sup>-3</sup> in order to fit the flux constraint at 4.5  $\mu$ m (Fig. 3). However, thermochemical equilibrium and photochemical models predict a CO<sub>2</sub> mixing ratio of

~10<sup>-7</sup> in hydrogen-dominated atmospheres at solar abundance (~10<sup>-5</sup> for 30 times solar metallicities)<sup>19,20</sup>.

We also explored other possibilities to explain the observations. A temperature inversion does not fit the data well because H<sub>2</sub>O and CH<sub>4</sub> would emit much more strongly than we observe in the 5.8- and 8.0- $\mu$ m channels, respectively. Non-local thermodynamic equilibrium emission from the dayside of exoplanet HD 189733b is attributed<sup>21</sup> to CH<sub>4</sub> fluorescence near 3.25  $\mu$ m. However, our 3.6- $\mu$ m detection is too strong to be explained by fluorescence alone. Alternatively, the methane deficiency could be explained by a lack of hydrogen; however, mass and radius constraints placed by transit and radial-velocity observations call for a hydrogen-dominated atmosphere<sup>7,8</sup>, which we explored above. Atmospheric compositions dominated by an alternative species (such as He or N<sub>2</sub>) are difficult to invoke plausibly. Hydrogen is the most abundant species in planet-forming disks and atmospheric escape rates are small for Neptune-mass planets. Although the observations were not made simultaneously, planet variability and stellar activity are unlikely explanations for our observations. A global, planetary temperature variation of 400 K manifesting in 2.64 days (the time between the 3.6- and 4.5- $\mu$ m observations) would be unprecedented in planetary science, as would a transient hot vortex<sup>22</sup> with one-third the planetary radius and T ≈ 2,200 K that appeared during only one of our six observations. Stellar activity, which is common among M dwarfs, would need to be timed precisely with the secondary eclipse for us not to detect and mask it.

The brown dwarf GJ 570D has an effective temperature similar to that of GJ 436b (800 K), but at atmospheric levels where T < 1,100 K, CH<sub>4</sub> is the dominant carbon-bearing molecule, with a CH<sub>4</sub>-to-CO ratio of ~10<sup>2</sup> (ref. 9). We estimate a ratio of ≤1 × 10<sup>-3</sup> for GJ 436b (Table 2); however, the exoplanet is strongly irradiated on one side, which can drive atmospheric dynamics and disequilibrium chemistry. Vertical mixing<sup>9</sup> can dredge CO up from deeper and hotter parts of the atmosphere, where CO is favoured, resulting in a small CH<sub>4</sub>-to-CO ratio if the rate of dredging is faster than the rate of the reaction that converts CO to CH<sub>4</sub> (CO + 3H<sub>2</sub> ↔ CH<sub>4</sub> + H<sub>2</sub>O). However, the observed CH<sub>4</sub>-to-CO mixing ratio would require large amounts of vertical mixing. Alternatively, CH<sub>4</sub> may be depleted by polymerization into hydrocarbons such as ethylene (C<sub>2</sub>H<sub>4</sub>). This is a major methane reaction pathway at these temperatures<sup>10</sup>. These possibilities represent starting points for future theoretical work with this atmosphere.

Received 18 November 2009; accepted 5 March 2010.

- Gillon, M. *et al.* Detection of transits of the nearby hot Neptune GJ 436 b. *Astron. Astrophys.* 472, L13-L16 (2007).

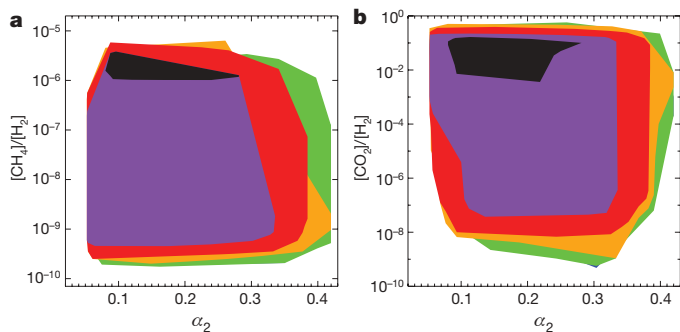


**Figure 3 | Contours showing the explored mixing ratios of methane.** The purple, red, orange and green contours show error surfaces within  $\chi^2$  of 1, 2, 3 and 4, where  $\chi^2$  is  $\chi^2$  divided by the number of channels<sup>18</sup>. We use the 3 $\sigma$  upper limit for the 4.5- $\mu$ m observation. The black surfaces show models with  $\chi^2 < 1$  and CH<sub>4</sub>/H<sub>2</sub> > 10<sup>-6</sup>. The figure demonstrates that models with CH<sub>4</sub> mixing ratios close to 10<sup>-6</sup> or above (a) require extremely large (>10<sup>-3</sup>) CO<sub>2</sub> mixing ratios (b), which are unphysical based on current understanding of CO<sub>2</sub> chemistry. The parameter space was explored with ~10<sup>6</sup> models. The  $\alpha_2$  parameter, which is related to the temperature gradient in the lower atmosphere<sup>18</sup>, was chosen arbitrarily for the abscissa.

2. Torres, G. The transiting exoplanet host star GJ 436: a test of stellar evolution models in the lower main sequence, and revised planetary parameters. *Astrophys. J.* **671**, L65–L68 (2007).
3. Deming, D. *et al.* Spitzer transit and secondary eclipse photometry of GJ 436b. *Astrophys. J.* **667**, L199–L202 (2007).
4. Demory, B.-O. *et al.* Characterization of the hot Neptune GJ 436 b with Spitzer and groundbased observations. *Astron. Astrophys.* **475**, 1125–1129 (2007).
5. Pont, F., Gilliland, R. L., Knutson, H., Holman, M. & Charbonneau, D. Transit infrared spectroscopy of the hot Neptune around GJ 436 with the Hubble Space Telescope. *Mon. Not. R. Astron. Soc.* **393**, L6–L10 (2009).
6. Burrows, A. & Sharp, C. M. Chemical equilibrium abundances in brown dwarf and extrasolar giant planet atmospheres. *Astrophys. J.* **512**, 843–863 (1999).
7. Figueira, P. *et al.* Bulk composition of the transiting hot Neptune around GJ 436. *Astron. Astrophys.* **493**, 671–676 (2009).
8. Rogers, L. A. & Seager, S. A framework for quantifying the degeneracies of exoplanet interior compositions. *Astrophys. J.* **712**, 974–991 (2010).
9. Saumon, D. *et al.* Ammonia as a tracer of chemical equilibrium in the T7.5 dwarf Gliese 570D. *Astrophys. J.* **647**, 552–557 (2006).
10. Zahnle, K., Marley, M. S. & Fortney, J. J. Thermometric soots on hot Jupiters? Preprint at (<http://arxiv.org/abs/0911.0728>) (2009).
11. Werner, M. W. *et al.* The Spitzer Space Telescope mission. *Astrophys. J. Suppl. Ser.* **154**, 1–9 (2004).
12. Ford, E. B. Quantifying the uncertainty in the orbits of extrasolar planets. *Astrophys. J.* **129**, 1706–1717 (2005).
13. Knutson, H. A., Charbonneau, D., Allen, L. E., Burrows, A. & Megeath, S. T. The 3.6–8.0  $\mu\text{m}$  broadband emission spectrum of HD 209458b: evidence for an atmospheric temperature inversion. *Astrophys. J.* **673**, 526–531 (2008).
14. Harrington, J., Luszcz, S., Seager, S., Deming, D. & Richardson, L. J. The hottest planet. *Nature* **447**, 691–693 (2007).
15. Deming, D., Seager, S., Richardson, L. J. & Harrington, J. Infrared radiation from an extrasolar planet. *Nature* **434**, 740–743 (2005).
16. Caceres, C. *et al.* High cadence near infrared timing observations of extrasolar planets: I. GJ 436b and XO-1b. *Astron. Astrophys.* **507**, 481–486 (2009).
17. Maness, H. L. *et al.* The M dwarf GJ 436 and its Neptune-mass planet. *Publ. Astron. Soc. Pacif.* **119**, 90–101 (2007).
18. Madhusudhan, N. & Seager, S. A temperature and abundance retrieval method for exoplanet atmospheres. *Astrophys. J.* **707**, 24–39 (2009).
19. Lodders, K. & Fegley, B. Atmospheric chemistry in giant planets, brown dwarfs, and low-mass dwarf stars. I. Carbon, nitrogen, and oxygen. *Icarus* **155**, 393–424 (2002).
20. Zahnle, K., Marley, M. S., Freedman, R. S., Lodders, K. & Fortney, J. J. Atmospheric sulfur photochemistry on hot Jupiters. *Astrophys. J.* **701**, L20–L24 (2009).
21. Swain, M. R. *et al.* A ground-based near-infrared emission spectrum of the exoplanet HD189733b. *Nature* **463**, 637–639 (2010).
22. Cho, J., Menou, K., Hansen, B. M. S. & Seager, S. Atmospheric circulation of close-in extrasolar giant planets. I. Global, barotropic, adiabatic simulations. *Astrophys. J.* **675**, 817–845 (2008).
23. Alonso, R. *et al.* Limits to the planet candidate GJ 436c. *Astron. Astrophys.* **487**, L5–L8 (2008).
24. Castelli, F. & Kurucz, R. L. New grids of ATLAS9 model atmospheres. Preprint at (<http://arxiv.org/abs/astro-ph/0405087>) (2004).
25. Bean, J. L., Benedict, G. F. & Endl, M. Metallicities of M dwarf planet hosts from spectral synthesis. *Astrophys. J.* **653**, L65–L68 (2006).
26. Swain, M. R. *et al.* Molecular signatures in the near-infrared dayside spectrum of HD 189733b. *Astrophys. J.* **690**, L114–L117 (2009).
27. Atreya, S. K., Mahaffy, P. R., Niemann, H. B., Wong, M. H. & Owen, T. C. Composition and origin of the atmosphere of Jupiter — an update, and implications for the extrasolar giant planets. *Planet. Space Sci.* **51**, 105–112 (2003).
28. Lodders, K. & Fegley, B. Jr. The origin of carbon monoxide in Neptune's atmosphere. *Icarus* **112**, 368–375 (1994).
29. Mandel, K. & Agol, E. Analytic light curves for planetary transit searches. *Astrophys. J.* **580**, L171–L175 (2002).
30. Reiners, A. Activity-induced radial velocity jitter in a flaring M dwarf. *Astron. Astrophys.* **498**, 853–861 (2009).

**Supplementary Information** is linked to the online version of the paper at [www.nature.com/nature](http://www.nature.com/nature).

**Acknowledgements** We thank the Spitzer staff for rapid scheduling; M. Gillon, A. Lanotte and T. Loredó for discussions; D. Wilson for contributed code; and A. Wright for manuscript comments. We thank the following for software: the Free Software Foundation, W. Landsman and other contributors to the Interactive Data Language Astronomy Library, contributors to SciPy, Matplotlib and the Python programming language, and the open-source community. This work is based on observations made with the Spitzer Space Telescope, which is operated by the Jet Propulsion Laboratory, California Institute of Technology, under a contract with NASA. This material is based on work supported by the US NSF and by the US NASA through an award issued by JPL/Caltech.

**Author Contributions** K.B.S. wrote the paper and Supplementary Information with contributions from J.H., N.M. and R.A.H.; N.M. and S.S. produced the atmospheric models; S.N., K.B.S. and W.C.B. reduced the data; K.B.S., J.H. and D.D. analysed the results; D.D. ran an independent analysis; R.A.H. produced the orbital parameter results; and J.H., K.B.S., S.N., R.A.H., E.R. and N.B.L. wrote the analysis pipeline.

**Author Information** The original data are available from the Spitzer Space Telescope archive, programs 30129 and 40685. Reprints and permissions information is available at [www.nature.com/reprints](http://www.nature.com/reprints). The authors declare no competing financial interests. Correspondence and requests for materials should be addressed to K.B.S. ([kevin218@knights.ucf.edu](mailto:kevin218@knights.ucf.edu)).